APPLIED SCIENCES AND ENGINEERING

# Toward all-day wearable health monitoring: An ultralow-power, reflective organic pulse oximetry sensing patch

**Hyeonwoo Lee, Eunhye Kim, Yongsu Lee, Hoyeon Kim, Jaeho Lee, Mincheol Kim, Hoi-Jun Yoo, Seunghyup Yoo***



**Pulse oximetry sensors have been playing a key role as devices to monitor elemental yet critical human health states. Conventional pulse oximetry sensors, however, have relatively large power consumption, impeding their use as stand-alone, continuous monitoring systems that can easily be integrated with everyday life. Here, we exploit the design freedom offered by organic technologies to realize a reflective patch-type pulse oximetry sensor with ultralow power consumption. On the basis of flexible organic light-emitting diodes and organic photodiodes designed via an optical simulation of color-sensitive light propagation within human skin, the proposed monolithically integrated organic pulse oximetry sensor heads exhibit successful operation at electrical power as low as 24 μW on average. We thereby demonstrate that organic devices not only have form factor advantages for such applications but also hold great promise as enablers for all-day wearable health monitoring systems.**

## INTRODUCTION

Digitized and continuous monitoring of biohealth signals is a key element for mobile health care, where a patient or a potential patient may receive an alert on changes to his or her health condition or seek medical advice from health care providers while remotely located from a hospital. The collected biohealth signals may carry even more profound implications by serving as a basis for medical "big data" that could identify unknown linkages between diseases and certain patterns of a given biohealth signal in a new medical era brought about by artificial intelligence. Photoplethysmogram (PPG) and peripheral oxygen saturation ($SpO_2$) signals are a good example of such biohealth signals that can benefit from continuous monitoring; they not only provide key information related to a person's vital state but also are expected to have potential links with other symptoms or physical conditions (*1*–*3*). Both signals can be measured simultaneously with a medical device called a "pulse oximeter," which generally consists of light sources in two different wavelengths and a photodetector that produces electrical signals modulated by the wavelength-dependent absorption of photons by oxygenated and nonoxygenated hemoglobin ($HbO_2$ and Hb) in blood vessels (*4*, *5*).

Being configured as either a transmissive or a reflective type, conventional pulse oximeters are based on inorganic light-emitting diodes (LEDs) made of III-V compound semiconductors and Si photodiodes (PDs). Even with the relatively high efficiency of LEDs, however, collecting a sufficient level of signal in these systems often requires a power consumption on the order of milliwatts (*6*, *7*), making it nontrivial to apply them to wearable devices that rely on batteries with a limited storage. As an alternative to inorganic-based conventional pulse oximeters, those based on organic LEDs (OLEDs) and organic photodiodes (OPDs) have recently been demonstrated (*8*–*14*). These pioneering works illustrated the potential of organic-based pulse oximeters for wearable sensors in that they can be configured in mechanically flexible and lightweight forms. However, the previous organic-based pulse oximeters focused more on the feasibility and/or on such form factor advantages. Little attention, on the other hand, has been paid to the potential of organic-based pulse oximeters in terms of ultraefficient operation to meet the challenging power demand of wearable applications.

In this work, we take full advantage of the design freedom offered by organic devices and, with the help of an optical analysis looking at color-sensitive light propagation within human skin, show that organic pulse oximeters (OPOs) can operate at as low as a few tens of microwatts—far less than the power typically required for their inorganic counterparts. This demonstrates that OPOs are promising with regard to not only form factors but also power consumption, and as such, they can be an outstanding candidate for stand-alone wearable devices ready for continuous, all-day monitoring.

## RESULTS

### Overview of the proposed OPO sensors

Figure 1A shows the overall layout of the proposed OPO sensor. It is based on a reflective configuration, and thus, light sources and detectors are on the same plane (*15*). This geometry allows pulse oximetry to be applied to a variety of pulsating surfaces of the human body so that they can easily be incorporated into common wearables such as smart watches and can later be combined with other types of sensors for integrated, multimodal health monitoring (*16*, *17*). This is in contrast with the case of their transmission-type counterparts, which can only be applied on terminal body parts such as the finger tips and earlobes, across which light transmittance can be substantial. As $SpO_2$ measurement requires two spectral light sources having the same and different extinction coefficients, respectively, between $HbO_2$ and Hb (*18*), we adopt a green (G) OLED for the former and a red (R) OLED for the latter (*11*–*13*, *19*). These devices are based on phosphorescent emitters (*20*, *21*), as shown in Fig. 1B, and exhibit high external quantum efficiency (EQE) with a relatively low roll-off even at a high brightness level, as shown in Fig. 1C (see section S1 and Table 1 for detailed OLED characteristics). It is noteworthy that commercial pulse oximetry sensors mostly adopt a near infrared (NIR) light source instead of a green light source because the former is less subject to absorption in the skin itself and thus has a longer

School of Electrical Engineering, Korea Advanced Institute of Science and Technology (KAIST), Daejeon 34141, Republic of Korea.
*Corresponding author. Email: syoo.ee@kaist.edu

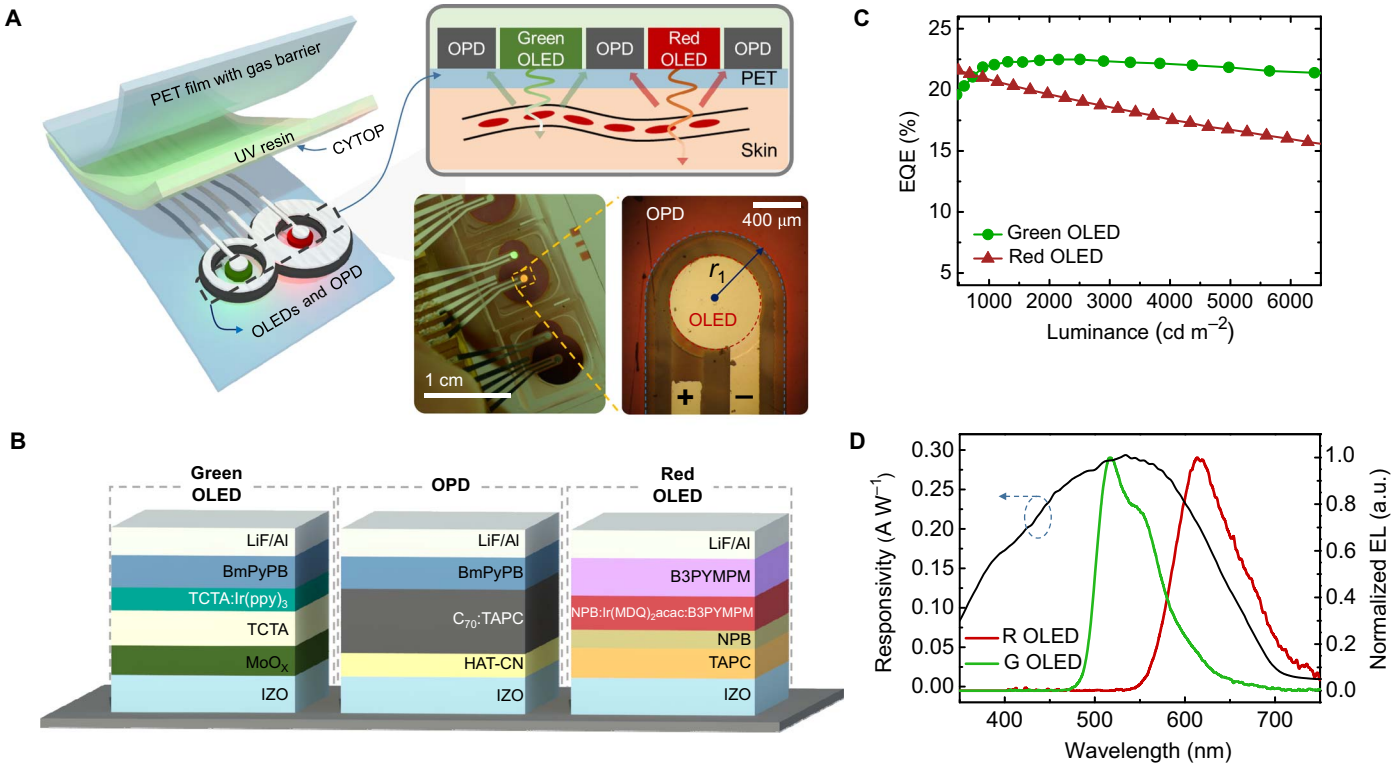


**Fig. 1. Overview of the proposed OPO sensors.** (**A**) Schematic of the proposed OPO sensor with enlarged cross-sectional view to depict device arrangement and light receiving process through the skin medium. The picture of an OPO sensor in operation is also shown. Note that the 8-shaped OPD wraps around red and green OLEDs in operation. A microscope image of a red OLED and a part of the neighboring OPD are presented to show device-to-device alignment and electrode arrangement. Photo Credit: Hyeonwoo Lee, KAIST. (**B**) The device structure of the green OLED, the OPD, and the red OLED used for the proposed OPO sensor. (**C**) EQE versus luminance characteristics of green and red OLEDs. The detailed current density (*J*)–voltage (*V*)–luminance (*L*) characteristics are represented in section S1. (**D**) Spectral responsivity of the proposed OPD at 0 V and spectral emission plot of the proposed OLEDs. The responsivity values at 520 and 610 nm, which are the peak wavelengths of the green and red OLEDs, are found to be 0.29 and 0.21 A/W, respectively. The detailed *J-V* curves of the OLEDs and the OPD are shown in section S1. a.u., arbitrary units.

**Table 1. Performance summary of OLEDs and OPD studied in this work.**

| OLED* | | | OPD*† | | |
|---|---|---|---|---|---|
| | Green | Red | | At λ = 520 nm | At λ = 610 nm |
| **EQE** (%) | 21.9 | 20.8 | ***R*** (A/W) | 0.29 | 0.21 |
| **Power efficiency** (lm W$^{-1}$) | 59.8 | 29.3 | $D^{*(ideal)}$ (Jones) | 4.3 × 10$^{12}$ | 3.1 × 10$^{12}$ |
| **Turn on voltage** (V) | 2.8 | 2.1 | $D^{*(typical)}$ (Jones) | 3.2 × 10$^{10}$ | 2.3 × 10$^{10}$ |

*The detailed device characteristics are presented in section S1. EQE and power efficiency values were measured at 1000 cd m$^{-2}$. †$D^*$ was estimated using the magnitude of dark current recorded at $V = -60$ mV and equivalent shunt resistance estimated from the dark *J-V* characteristics. For details on the estimation of $D^*$, please refer to the description provided in section S1.

travel length within the skin; nevertheless, G OLED is chosen because efficient NIR organic emitters are still in the developmental stages (*22*, *23*), as was discussed in previous works (*11*, *12*). For a photodetector, we adopt an OPD based on an active layer of $C_{70}$ mixed with 4,4′-cyclohexylidenebis[*N*,*N*-bis(4- methylphenyl)benzenamine] (TAPC) in a 20:1 ratio, as shown in Fig. 1B. This type of device is known to work efficiently as a photovoltaic device (*24*, *25*) and also as a PD (*26*). Responsivity values of the OPD used in this study at the peak wavelengths of the R and G OLEDs in Fig. 1B are 0.21 A/W (at 610 nm) and 0.29 A/W (at 520 nm), respectively, at a zero bias condition, and these values are comparable to those of Si-based PDs. Specific detectivity ($D^*$) values are estimated at $V = -60$ mV to be 3.1 × 10$^{12}$ Jones (at 610 nm) and 4.3 × 10$^{12}$ Jones (at 520 nm) for ideal, shot noise limited characteristics assumed, and to be 2.3 × 10$^{10}$ Jones (at 610 nm) and 3.2 × 10$^{10}$ Jones (at 520 nm) for typical operation conditions relevant to the present case, where devices are to be attached onto a human body held at the body temperature of ca. 310 K and thus the noise current is dominated by thermal, i.e., Johnson noise (see Fig. 1D, Table 1, and section S1 for OPD characteristics).

### Design considerations for low-power OPO sensors

As with transmissive OPO sensors, the success of reflective OPO sensors heavily relies on whether a sufficient amount of light can be delivered from light sources to a detector after propagating through a certain portion of human skin that includes arterial blood vessels. In this context, previous works on reflection-type OPOs also made efforts to enhance light coupling from light sources to a detector; for example, Han *et al.* experimentally searched for the optimal distance between a discrete PD and printed polymer LEDs, and Yokota *et al.* designed an organic PD in a circular shape where each side was surrounded by semicircular red and green OLEDs so that more light from the OLEDs would be coupled to the OPD (*12*, *13*). However, design based on a full optical modeling has not been done for reflective $SpO_2$ sensors, mainly due to the complexities involved in optical analysis of light propagation within the skin, which involves both absorption and scattering from various organelles. The device layout proposed in this work places circular red and green OLEDs with radii as small as 0.4 mm side by side and wraps them around a single OPD that resembles the number "8," as shown in Fig. 1A. In this way, light generated from an OLED can be coupled to the OPD in almost all directions so that the chance of wasting light can be minimized to a significant degree. In this geometry, the OPD is shared by the two OLEDs, making it possible to keep the overall size of the $SpO_2$ sensor unit compact and to maintain its interconnection and transimpedance circuitry to be simple. It is noteworthy that such a monolithic integration and device layout is easily realized with organic semiconductor technology due to its simple fabrication route based on a shadow masking technique used in this work or the printing method adopted by Arias and her coworkers (*13*).

The spatial extent of the part of the OPD near the R or G OLED is individually determined for each of the red and green OLEDs, considering the color-dependent spatial distribution of optical power per unit area [$=f_H(r)$] at the surface of human skin at a distance of $r$ from the center of each OLED, for light that propagates through human skin and returns to its surface via multiple scattering events. To estimate $f_H(r)$ and thus optimize the dimensions of the OPD in Fig. 1A, we herein analyze light propagation from a small OLED facing human skin by adopting an optical skin model that follows Tuchin and co-workers (*27*, *28*), as schematically shown in Fig. 2A. The model considers human skin as a stratified medium through the layers of which light passes while experiencing either scattering or absorption. Scattering results largely from the interaction of light with various organelles such as mitochondria and lysosomes. As they typically have spherical or spheroidal shapes, with dimensions ranging from a few hundred nanometers to a few micrometers, the major scattering mechanism within human skin can be considered, to a good approximation, to follow Mie scattering with an asymmetry parameter ($g$) close to 0.7 to 1 (*29*, *30*). Although Mie scattering is rather spectrally neutral, spectral dependence of absorption can influence $f_H(r)$ depending on the wavelength ($\lambda$) of light. Figure 2 (B and C), which compares photons originating from R and G OLEDs, respectively, do indicate that $f_H(r)$ of G and R OLEDs drops differently with $r$,

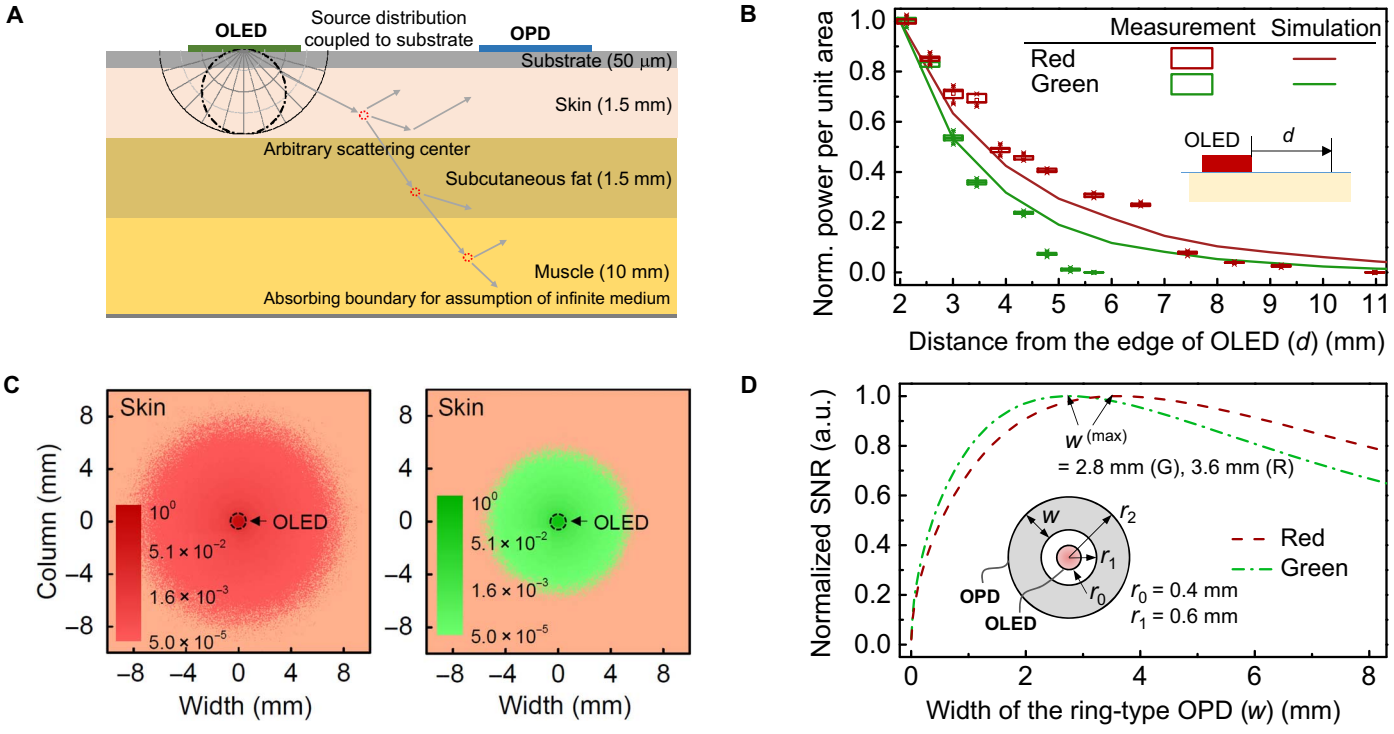


**Fig. 2. Design considerations for low-power OPO sensors.** (**A**) Schematic of the proposed optical skin model used in this study. (**B**) Measured and simulated normalized power measured at a distance measured from the edge of an OLED. Box and line charts represent experimental and simulation results, respectively. (**C**) Top view of the simulated optical power distribution at the surface of a skin. The light from each OLED is optically coupled to the skin and scatters from various organelle back to the top surface. The radius of each OLED ($r_0$) is set at 0.4 mm. (**D**) Calculated normalized signal-to-noise ratio (SNR) versus the width ($W$) of the concentric, ring-type OPD for light originating from a circular OLED with $r_0$ = 0.4 mm. The inner radius ($r_1$) of the ring-type OPD is set at $r_0$ + 0.2 mm (= 0.6 mm) in consideration of fabrication margin. The SNR values obtained here are with $f_H(r=r_1)$ and $I_0$ of 0.01 W/m$^2$ and 2.3 mm for red and 0.01 W/m$^2$ and 1.8 mm for green OLEDs. For details on estimation of SNR, refer to section S3.

for both experimentally obtained and simulated data. Let us assume that $f_H(r)$ for each color follows an exponential decay function with a characteristic lateral propagation distance ($l_0$), after propagation of which $f_H(r)$ reduces to $1/e$ (=37%) of the original value. $l_0$ in this case is ca. 1.8 mm for light from the G OLED (λ = 520 nm) and ca. 2.3 mm for light from the R OLED (λ = 610 nm) (see section S2 for details of the optical simulation and parameters used in the optical analysis). This result is consistent with the tendency that light with a longer wavelength travels farther inside the skin than that with a shorter wavelength (*30*).

Once $f_H(r)$ is identified for each color, one can estimate how many photons can be coupled into a ring-type OPD that wraps around a circular OLED and thus how large the photocurrent ($I_{PH}$) of the OPD can be. With the spectral responsivity of the OPD set as $R_{PD}(\lambda)$, $I_{PH}$ is given for the concentric geometry shown in the inset of Fig. 2D by

$$I_{PH}^{(i)} \approx 2\pi\int_{r_1}^{r_2} R_{PD}(\lambda_i) f_H(r;\lambda_i) r dr (i = \text{R or G}) \quad (1)$$

where $r_1$ and $r_2$ are the inner and outer radii of the ring-type OPD; $\lambda_i$ is the peak wavelength of an OLED, with $i$ being an index referring to either a red (R) or a green (G) OLED. As $(r_2 - r_1)$ (= $w$) increases from zero with $r_1$ fixed, both $I_{PH}^{(i)}$ and the noise current [= $I_{tn}^{(i)}$] increase in proportion to the area of the OPD [= $A_{PD} = \pi(r_2^2 - r_1^2)$] and $A_{PD}^{0.5}$, respectively, until $w$ reaches approximately $l_0^{(i)}$ of an OLED, with $i$ being R or G (see section S3). Once $w$ becomes much larger than $l_0^{(i)}$, however, $I_{PH}^{(i)}$ tends to be saturated without a further significant increase because there are only a limited number of photons at a distance from the source beyond several $l_0$'s. On the other hand, the noise current continues to increase with $A_{PD}^{0.5}$. For this reason, the SNR gets maximized at $w^{(i)}$ close to $\beta l_0^{(i)}$, with β in the range of 1 to 2, as can be confirmed in Fig. 2D, for typical conditions. Likewise, too large an OLED would waste many of the photons because light emitted from the center of the OLED, for example, may not necessarily be collected by an OPD adjacent to it. In addition, one may note that there can be other possibilities for optimal designs. Examples include a design that places vertically stacked R and G OLEDs at the center of a ring-shaped OPD or a design that places R and G OLEDs closely side by side at the center of a ring-shaped OPD. While both of these examples could result in further reduction in the overall dimension, care must be taken in consideration of possible efficiency changes associated with the introduction of stacking geometry and, fabrication and interconnection margins, etc.

## Fabrication and characterization of OPO sensors

On the basis of the design considerations summarized above, we fabricated OPO sensors in the geometry shown in Fig. 1A on a 50-μm-thick polyethylene terephthalate (PET) substrate with precoated barrier layers (MS-F2050PAC, LINTEC Corporation) with $r_2^{(G)}$ and $r_2^{(R)}$ set at 1.75 and 2.90 mm, respectively, and $r_1$ set at 0.6 mm for both R and G OLEDs (see section S4 for the overall fabrication process of OPOs). Note that $w^{(i)}$ [= $r_2^{(i)} - r_1^{(i)}$] in this case was chosen to be smaller than the corresponding optimal value obtained in the previous section for the concentric geometry. This choice was made in consideration of (i) the overall compactness and (ii) the 8-shaped design, which differs from the pure concentric geometry, for an OLED/OPD pair with a given color, in that it has an additional OPD portion surrounding an OLED with the other color. The latter ensured the SNR would remain large enough by preventing the total OPD area (and thus $I_{tn}$) from getting too large.

These devices were encapsulated in a so-called "face seal" configuration where the barrier-coated PET (50 μm in thickness) identical to that used for a substrate was placed over the devices, with ultraviolet (UV)–curable resin (XNR5570, Nagase ChemteX Corporation) covering the whole device. Before casting the resin, a fluorinated polymer called "CYTOP" (Asahi Glass) was spin coated on top of the organic devices to prevent resin from damaging the underlying organic layers. With the water vapor transmission rate of the barrier-coated PET rated at $5 \times 10^{-4}$ g/m$^2$ per day, these encapsulated devices exhibit a storage lifetime longer than 10 days (27°C, relative humidity, 47%), which is more than adequate for a field test in ambient air (see section S5 for the fabrication process and stability of the encapsulated devices). The whole device structure was monolithically integrated within a 1-cm$^2$ area so that it can eventually be applied onto various body parts. We achieved such compactness and tight relative alignment among R and G OLEDs and the 8-shaped OPD by using a "mask-in-mask" method, in which shadow masks with desired patterns were plugged snuggly into a magnetically held guide mask as in a jigsaw puzzle (see fig. S4C). In this manner, relative alignment was accomplished with a lateral gap as low as 100 μm.

The completed OPO sensors were then placed against various body parts such as fingers, wrist, neck, and nose to validate their proper operation (see fig. S6 for photographs). The OPO sensors were operated with a battery-powered custom-designed circuit board (Healthrian Co. Ltd.) that contains an integrated analog front-end (AFE) chip (AFE4403, Texas Instruments Inc.), a DC-DC converter to deal with a wide range of operating voltage, a microcontroller, and a communication input/output. The AFE chip consists mainly of a LED current driver, a PD receiver containing a transimpedance amplifier (TIA), ambient light rejection, a built-in low-pass filter (LPF) with a 3dB cutoff frequency ($f_{3dB}$) of 500 Hz, and an analog-to-digital converter (ADC). R and G OLEDs of the OPO sensors were driven alternatively at a sampling rate of 200 Hz at a 25% duty cycle. The OPD output signal was then collected with the TIA of AFE and passed through the built-in LPF onto the ADC for further communication with other digital devices (see section S7 for details on the circuit board). The output signal from the circuit board was further digitally processed with a software-based LPF (a 10th-order Butterworth filter) with $f_{3dB}$ of 5 Hz, and an optional period moving average filter (*31*) was used to deal with noise induced by motion and/or ambient light and simple white noise. With the low-frequency bandwidth inherent to the PPG signal, low-pass filtering effectively kept the noise level sufficiently low, as illustrated in section S7. To ensure accurate $SpO_2$ measurement, we calibrated the OPO sensor with respect to $SpO_2$ values taken concurrently by a commercial forceps-type transmissive pulse oximeter (see section S8 for details). As shown in Fig. 3A, reliable signals for both heart rate and $SpO_2$ were obtainable in all the tested body parts. With the noise processing and the proposed optical design for highly efficient use of light, these signals were achieved with driving current as low as 25 μA at 5 V for G OLED and 21 μA at 3.3 V for R OLED. With the duty cycle of 25% (100 %), these driving conditions correspond to effective power consumption of 31 μW (125 μW) for G and 17 μW (68 μW) for R, respectively. It is noteworthy that these values correspond to the lowest power usage among the pulse oximetry sensors reported to date including those based on OLEDs and LEDs with the same duty ratio. The low power operation of the proposed OPO sensor (= PO0) is well illustrated in a comparison experiment carried out with a homemade

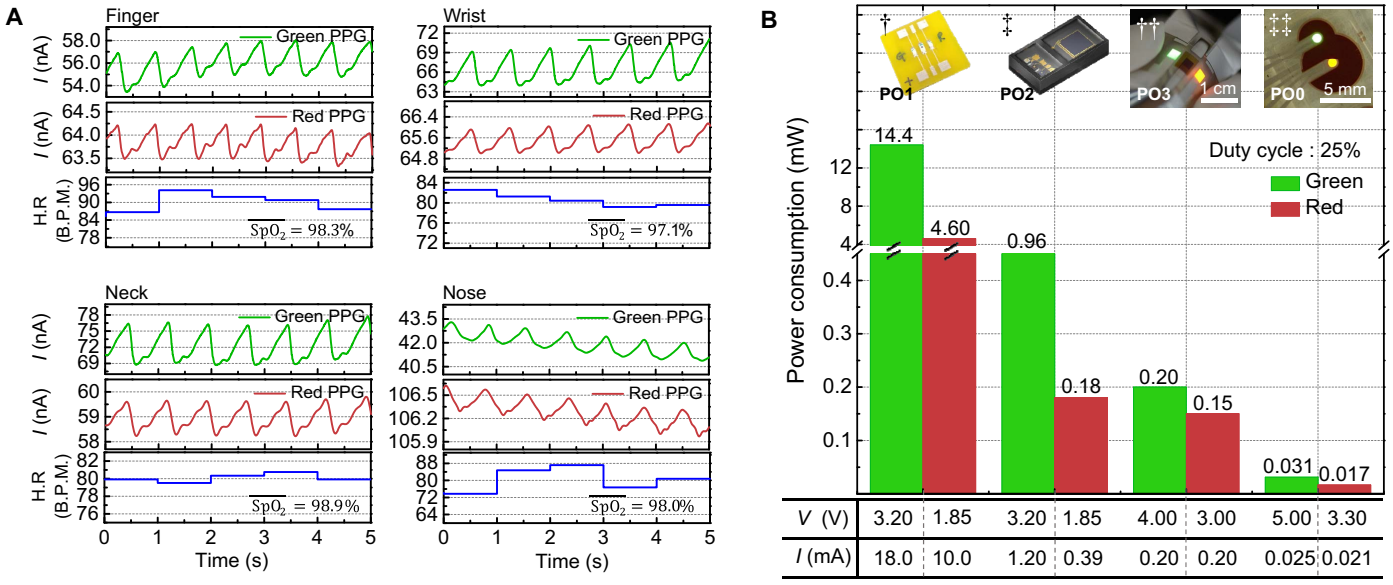


**Fig. 3. OPO sensor measurement at various body parts and power consumption comparison.** (**A**) The PPG signal, heart rate, and $SpO_2$ value obtained with R and G OLEDs from various body parts. H.R, heart rate; B.P.M., beats per minute. (**B**) Comparison of the power consumption of R and G light sources of oximetry sensors compared: †, discrete optical elements integrated on a PCB substrate with the edge-to-edge distance between elements being 2 mm (= PO1); ‡, a commercially available reflective pulse oximetry head (SFH7050, Osram Sylvania Inc.) (= PO2); ††, OPO sensor wherein rectangular OLEDs and OPDs are arranged side by side with the edge-to-edge distance of 2 mm (= PO3); ‡‡, the OPO sensor proposed in this work (= PO0). The layer configurations of OLEDs and OPD in the OPO sensor used in †† are identical to those used in this work.Photo Credit: Hyeonwoo Lee, KAIST.

pulse oximetry sensor based on discrete R- and G-LEDs and a Si PD (= PO1), and a commercially available off-the-shelf reflective PO sensor (SFH7050, Osram Sylvania Inc.) (= PO2), the same OPO sensor as the proposed one except for larger dimension and linear arrangement of the OLEDs with an OPD placed between them, as shown in the inset of Fig. 3B (= PO3) (*14*). Even in consideration of room for further optimization for each type of sensor, the order-of-magnitude difference in driving power measured for the similar level of $I_{PH}$ demonstrates the advantage of the proposed OPO sensors.

## DISCUSSION

In addition to the efficient use of photons enabled via a high degree of design freedom offered by organic device technology, one should further note the significance of refractive index matching between the substrate of an OPO device and human skin. In a typical bottom-emitting OLED, many of the photons generated from the active layer are confined within its substrate due to total internal reflection, and their relative portion (= $\eta_{sc}$) can be as large as ca. 30 to 35%. This is even higher than the portion of the photons directly outcoupled to air (= $\eta_{air}$), which is at best about 20% for isotropic dipole emitters. When the refractive index of the substrate is perfectly matched to that of the skin, ($\eta_{sc} + \eta_{air}$) of the photons generated inside the active layer can theoretically be coupled into the skin. Hence, properly index-matched operation makes OLEDs much more advantageous for OPO sensors than conventional air-coupled operation, in terms of efficient use of photons. Because of the conformal nature of flexible devices, independent experiments done with a bottom-emitting OLED (active area, 4 $mm^2$) indicate that the optical power monitored from the edge of the substrate is reduced by approximately 32% when the front part of the device is in contact with the bottom of a finger, as shown in Fig. 4A. This reduction is attributable to contact-induced light extraction of the substrate-confined photons. As shown in Fig. 4B, this value may be compared with almost 90% extraction of the substrate-confined light by a half-ball lens and with ca. 56% extraction by a microlens array (MLA). The major difference is expected to come from (i) the limited contact area between the palm of a finger and the OLED surface; (ii) photons that reenter the substrate after being backscattered inside the skin; and/or (iii) the corrugations present in the finger that further limit the contact area. The use of index-matching fluid between the finger and the substrate increased the reduction to ca. 40%, indicating that an approximately 10% difference may come from the corrugations. Although less effective than typical extraction films, contact-induced outcoupling of substrate-confined modes is still significant enough to help efficient use of photons generated from OLEDs in OPO sensors; with $\eta_{air}$ = 20% and $\eta_{sc}$ = 30%, for example, the ratio of photons coupled into the skin can be approximately 30% ($\approx \eta_{air} + 0.32 \times \eta_{sc}$), which is a 50% relative enhancement with respect to $\eta_{air}$.

Furthermore, index matching between the substrate and the OLED plays an additional role by preventing light from the OLED from being coupled directly to the OPD without going through the skin. The DC component associated with this directly coupled light, if significant, will overshadow small signals obtained from light propagating within the skin. When there is an air gap between the substrate and the skin, the amount of light delivered to a PD can become much larger, but most of the signal will come mainly from the rays guided within the substrate, not from those that pass through the skin and return (Fig. 4, C and D). It is also noted that the present simulation is not able to separate photons that meet blood vessels in their passage from those which do not. If the latter is greater, it could also bury the former, which forms a meaningful signal. Development of such a simulation that can tell them apart would be of help in elucidating what is happening below human skin to make reflective PPG sensing readily available. It can at least be seen in fig. S2 that many of the rays go deep

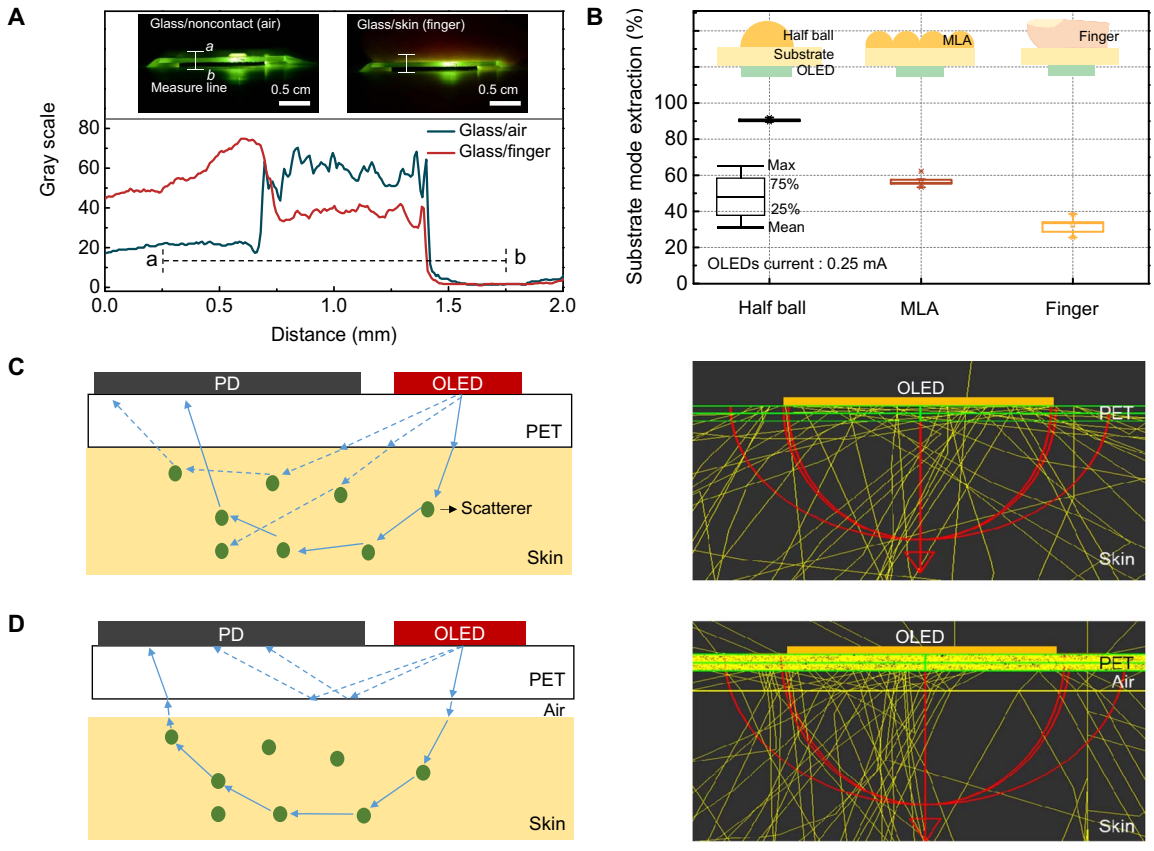


**Fig. 4. Significance of the optical coupling between the OPO sensor and the skin.** (**A**) Optical coupling monitored via reduction in substrate-confined light in the OLED. Spatial distribution of light seen across the edge of the substrate in the presence or absence of a finger contact on the OLED-emitting surface. Insets are side-view snapshots of the OLED glass/air and OLED glass/finger, respectively. Photo Credit: Hyeonwoo Lee, KAIST. (**B**) Extraction of substrate-confined mode from an OLED versus outcoupling methods shown in the inset diagrams: half-ball lens, MLA, and finger contact. (**C** and **D**) Cross-sectional view of ray diagrams: illustration (left) and optical simulation results (right) for the case where the substrate (PET) is optically coupled to the skin (C) and for the case where the substrate is not optically coupled to the skin due to the presence of air gap between the substrate and the skin (D).

below the skin layer. The reason why those rays can return after the deep propagation to the OPD that is rather close to the OLED is believed to come from the random nature of scattering that tends to spread out the lateral light distribution.

Containing two relatively thick substrates for encapsulation, the present OPOs under study have a limited degree of flexibility; this is not a big problem for a reflective-type OPO because, unlike transmissive-type OPOs, it does not have to be wrapped around at a tight bending radius. Nevertheless, sensors have to be gently pressed against the skin to ensure full conformal contact in the present case. Development of highly flexible devices based on ultrathin substrates, termed as "imperceptible electronic devices" (*32*), may be of help not only for their imperceptible nature but also for significantly enhanced conformal contact between the sensors and the skin. The work is currently under way based on ultrathin substrates and thin-film encapsulation.

In summary, we realized a reflective patch-type, OPO sensor with ultralow power consumption based on flexible OLEDs and OPDs. Through an optical simulation of color-sensitive light propagation associated with scattering and absorption that occurs within human skin, an ideal OPD wraparound layout has been proposed where the OPD resembling the number 8 wraps around small circular OLEDs for each red and green emission. With this approach, the proposed monolithically integrated OPO sensors exhibited successful operation at electrical power as low as a few tens of microwatts on top of various body parts. The conformal, index-matched contact between the substrate and the skin makes it possible to access and use a significant amount of light that would otherwise be confined within the substrate. It was also shown that this index matching is important for suppression of direct coupling of light between an OLED and an OPD. The results presented here illustrate that organic devices not only have form factor advantages but also hold great promise as enablers for all-day wearable health monitoring systems. Furthermore, the main idea presented here can be further extended to PPG or $SpO_2$ sensors based on inorganic LEDs and PDs (*33*), for example, via novel techniques developed for transfer of thin, micropatterned inorganic optoelectronic devices onto flexible substrates (*34*–*37*).

## MATERIALS AND METHODS

### OLED and OPD fabrication and evaluation

Indium zinc oxide (IZO) layers were prepared on precleaned PET (MS-F2050PAC, LINTEC Corporation) substrates with radio frequency (RF) sputtering (RF power, 120 W) in a vacuum ($6 \times 10^{-3}$ Torr). The IZO-coated PET substrates were cleaned with isopropyl alcohol in an ultrasonic bath and kept in a vacuum oven (60°C) for degassing for 6 hours before deposition. All substrates were treated by air plasma for

1 min in a plasma cleaner (CUTE-MP, Femto Science). The substrates were loaded into a vacuum chamber (HS-1100, Digital Optics & Vacuum) for thermal evaporation of organic and metal layers in ca. $1 \times 10^{-6}$ Torr. As can be seen in Fig. 1B, the proposed OLED devices had the following structures: (i) for a green OLED, PET/IZO (90 nm)/$MoO_3$ (10 nm)/tris(4-carbazoyl-9-ylphenyl) amine (TCTA; 30 nm)/TCTA:Ir(ppy)$_3$ [8 weight % (wt %), 20 nm]/1,3-bis[3,5-di(pyridin-3-yl)phenyl]benzene (BmPyPB; 60 nm)/LiF (1 nm)/Al (100 nm); (ii) for a red OLED, PET/IZO (90 nm)/TAPC (75 nm)/*N*,*N*′-Di(1-naphthyl)-*N*,*N*′-diphenyl benzidine (NPB; 10 nm)/NPB:4,6-bis(3,5-di(pyridin-3-yl)phenyl)-2-methylpyrimidine (B3PYMPM):9 wt % Ir(MDQ)$_2$acac (30 nm)/B3PYMPM (55 nm)/LiF (1 nm)/Al (100 nm). Ir(ppy)$_3$ and Ir(MDQ)$_2$acac refer to tris[2-phenylpyridinato-C2,N] iridium(III) and bis(2-methyldibenzo[f,h]quinoxaline) (acetylacetonate) iridium(III), respectively. The OPD device had the device structure of PET/IZO (90 nm)/HAT-CN (10 nm)/$C_{70}$:TAPC (4 wt %, 50 nm)/BmPyPB (10 nm)/LiF (1 nm)/Al (100 nm), wherein HAT-CN refers to 1,4,5,8,9,11-hexaazatriphenylenehexacarbonitrile.

The *J*-*V*-*L* characteristics and spectra of the OLED devices were obtained by a customized measurement setup consisting of a Keithley 2400 source meter, a calibrated PD (FDS100, Thorlab), and a fiber optic spectrometer (EPP2000, StellarNet), both of which are held in a motorized goniometer. The EQE and power efficiency of the devices were calculated from the current density, PD current, luminance, electroluminescence (EL) spectra, and angular distribution of EL intensity. The *J*-*V* characteristics of the OPD devices were measured with a source measure unit (Keithley 238). EQE and responsivity were measured under the DC mode using a photovoltaics (PV) spectral response measurement system (CEP-25ML, Bunkoukeiki). The irradiance of monochromatic lights was set at a constant value (50 μW cm$^{-2}$) with an irradiation area of 5 cm × 5 cm having spatial variation under 2.5%. All measurements for unencapsulated OPDs were measured inside a small vacuum chamber, which has a quartz window for light transmission.

### Face seal encapsulation process

After fabricating the OLEDs and OPDs constituting the proposed OPOs, face seal encapsulation was performed to protect the organic semiconductor devices, which are vulnerable to moisture and oxygen around them. A CYTOP solution (CTL-809M, Asahi Glass, Chiyoda, Japan) layer was deposited on the OPOs' active area by spin coating (500 rpm for 10 s and then 2000 rpm for 30 s); these samples were annealed on a hotplate at 70°C for 3 hours in a $N_2$-filled glove box. Before depositing the CYTOP layer, PDMS (polydimethylsiloxane) was placed along the edge of the OPO to prevent the contact electrode from being covered by the CYTOP. After CYTOP coating, ca. 80-μm-thick UV curable resin (XNR5570, Nagase ChemteX Corporation) was prepared on another barrier PET film by spin coating (500 rpm for 30 s and then 3000 rpm for 120 s), which was laminated onto the OPO. The resin was then UV-cured in a $N_2$-filled glove box (see fig. S5A).

### Optical skin modeling

Optical skin modeling was done with the commercial LightTools program by treating human skin as a stratified optical medium with embedded spheroid scatterers where the light could be scattered or absorbed (*27*, *28*). Over 1,000,000 rays were traced after starting from the green or red OLED sources. For the sake of simplicity, the probability distribution of angular deviation for Mie scattering was approximated to the Henyey-Greenstein (H-G) phase function (*29*, *30*). The detailed parameters used for simulations are provided in section S2. This study and all experiments performed on human subjects were performed with consent under the exemption approval of the KAIST Institutional Review Board.

## SUPPLEMENTARY MATERIALS

Supplementary material for this article is available at http://advances.sciencemag.org/cgi/content/full/4/11/eaas9530/DC1

Section S1. Device characteristics of OLEDs and OPDs
Section S2. Detailed description on optical simulation
Section S3. Estimation of SNR ratio in a concentric configuration where a circular OLED is surrounded by a ring-type OPD sharing the center
Section S4. Summary of overall fabrication process and mask-in-mask concept used for precise alignment among different patterns during thermal evaporation
Section S5. Face seal encapsulation and interconnection procedure and characteristics of encapsulated OLEDs and OPDs
Section S6. Application of proposed OPOs onto various body parts
Section S7. Driving and signal acquisition scheme
Section S8. $SpO_2$ calibration method for OPOs
Fig. S1. Opto-electrical characteristics of OLEDs and OPDs used in this work.
Fig. S2. Ray-tracing example of the proposed simulation model.
Fig. S3. Estimation of photo current, total noise, and SNR (= $I_{PH}/I_{tn}$) of each OLED case.
Fig. S4. Overview of fabrication process and pattern definition by jigsaw puzzle–type, mask-in-mask shadow masking method.
Fig. S5. Encapsulation and interconnection process and characteristics of the encapsulated devices.
Fig. S6. Pictures of the working OPO sensors taken on the various body parts.
Fig. S7. Schematic diagram showing the circuit functional blocks for driving of OLEDs and signal acquisition from the OPD of the proposed OPO sensors.
Fig. S8. Overview of the calibration method.
Fig. S9. Example of $SpO_2$ calibration done at a forefinger.
Table S1. Parameters used to estimate $D^*$ of the OPD under study.
Table S2. Optical parameter of the human skin layers applied to the simulation.
References (*38*, *39*)

## REFERENCES AND NOTES


1. J. Allen, Photoplethysmography and its application in clinical physiological measurement. *Physiol. Meas.* **28**, R1–R39 (2007).
2. H.-M. Lee, D.-J. Kim, H.-K. Yang, K.-S. Kim, J.-W. Lee, E.-J. Cha, K.-A. Kim, Human sensibility evaluation using photoplethysmogram (PPG), 2009 International Conference on Complex, Intelligent and Software Intensive Systems, CISIS 2009, Fukuoka, Japan, 16 to 19 March 2009 (IEEE, 2009), 149–153.
3. E. Gil, R. Bailón, J. M. Vergara, P. Laguna, PTT variability for discrimination of sleep apnea related decreases in the amplitude fluctuations of PPG signal in children. *IEEE Trans. Biomed. Eng.* **57**, 1079–1088 (2010).
4. Y. Mendelson, Pulse oximetry: Theory and applications for noninvasive monitoring. *Clin. Chem.* **38**, 1601–1607 (1992).
5. K. K. Tremper, Pulse oximetry. *Chest* **95**, 713–715 (1989).
6. P. K. Baheti, H. Garudadri, An ultra low power pulse oximeter sensor based on compressed sensing, BSN '09 Proceedings of the Sixth International Workshop on Wearable and Implantable Body Sensor Networks, Washington, DC, 3 to 5 June 2009 (IEEE, 2009), 144–148.
7. S. Rhee, B. H. Yang, H. H. Asada, Artifact-resistant power-efficient design of finger-ring plethysmographic sensors. *IEEE Trans. Biomed. Eng.* **48**, 795–805 (2001).
8. M. Koetse, P. Rensing, G. van Heck, R. Sharpe, B. Allard, F. Wieringa, P. Kruijt, N. Meulendijks, H. Jansen, H. Schoo, In plane optical sensor based on organic electronic devices, Organic Field-Effect Transistors VII and Organic Semiconductors in Sensors and Bioelectronics, San Diego, CA, USA, 10 to 12 August 2008.
9. J. Smith, E. Bawolek, Y.-K. Lee, B. O'Brien, M. Marrs, E. Howard, M. Strnad, J. M. B. Christen, M. Goryll, Application of flexible flat panel display technology to wearable biomedical devices. *Eletron. Lett.* **51**, 1312–1314 (2015).
10. Y. Chuo, B. Omrane, C. Landrock, J. N. Patel, B. Kaminska, Platform for all-polymer-based pulse-oximetry sensor, in *Sensors, 2010 IEEE* (IEEE, 2010), pp. 155–159.
11. C. M. Lochner, Y. Khan, A. Pierre, A. C. Arias, All-organic optoelectronic sensor for pulse oximetry. *Nat. Commun.* **5**, 5745 (2014).
12. T. Yokota, P. Zalar, M. Kaltenbrunner, H. Jinno, N. Matsuhisa, H. Kitanosako, Y. Tachibana, W. Yukita, M. Koizumi, T. Someya, Ultraflexible organic photonic skin. *Sci. Adv.* **2**, e1501856 (2016).

13. D. Han, Y. Khan, J. Ting, S. M. King, N. Yaacobi-Gross, M. J. Humphries, C. J. Newsome, A. C. Arias, Flexible blade-coated multicolor polymer light-emitting diodes for optoelectronic sensors. *Adv. Mater.* **29**, 1606206 (2017).
14. Y. Lee, H. Lee, J. Jang, J. Lee, M. Kim, J. Lee, H. Kim, S. Yoo, H.-J. Yoo, Sticker-type hybrid photoplethysmogram monitoring system integrating CMOS IC with organic optical sensors. *IEEE J. Emerg. Top. Circ. Syst.* **7**, 50–59 (2017).
15. T. Tamura, Y. Maeda, M. Yoshida, Wearable photoplethysmographic sensors—Past and present. *Electronics* **3**, 282–302 (2014).
16. V. Goverdovsky, D. Looney, P. Kidmose, C. Papavassiliou, D. P. Mandic, Co-located multimodal sensing: A next generation solution for wearable health. *IEEE Sens. J.* **15**, 138–145 (2015).
17. G. Cohen, P. de Chazal, Automated detection of sleep apnea in infants: A multi-modal approach. *Comput. Biol. Med.* **63**, 118–123 (2015).
18. M. W. Wukitsch, M. T. Petterson, D. R. Tobler, J. A. Pologe, Pulse oximetry: Analysis of theory, technology, and practice. *J. Clin. Monit.* **4**, 290–301 (1988).
19. G. A. Millikan, The oximeter, an instrument for measuring continuously the oxygen saturation of arterial blood in man. *Rev. Sci. Instrum.* **13**, 434–444 (1942).
20. K.-H. Kim, S. Lee, C.-K. Moon, S.-Y. Kim, Y.-S. Park, J.-H. Lee, J. W. Lee, J. Huh, Y. You, J.-J. Kim, Phosphorescent dye-based supramolecules for high-efficiency organic light-emitting diodes. *Nat. Commun.* **5**, 4769 (2014).
21. J. Lee, T.-H. Han, M.-H. Park, D. Y. Jung, J. Seo, H.-K. Seo, H. Cho, E. Kim, J. Chung, S.-Y. Choi, T.-S. Kim, T.-W. Lee, S. Yoo, Synergetic electrode architecture for efficient graphene-based flexible organic light-emitting diodes. *Nat. Commun.* **7**, 11791 (2016).
22. K. T. Ly, R.-W. Chen-Cheng, H.-W. Lin, Y.-J. Shiau, S.-H. Liu, P.-T. Chou, C.-S. Tsao, Y.-C. Huang, Y. Chi, Near-infrared organic light-emitting diodes with very high external quantum efficiency and radiance. *Nat. Photonics* **11**, 63–68 (2017).
23. T. Yamanaka, H. Nakanotani, S. Hara, T. Hirohata, C. Adachi, Near-infrared organic light-emitting diodes for biosensing with high operating stability. *Appl. Phys. Express* **10**, 074101 (2017).
24. M. Zhang, H. Wang, H. Tian, Y. Geng, C. W. Tang, Bulk heterojunction photovoltaic cells with low donor concentration. *Adv. Mater.* **23**, 4960–4964 (2011).
25. H. Kim, J. Chung, J. Ha, S. Yoo, Optimization of $C_{70}$:TAPC-based OPVs with IZO transparent Electrodes, The 13th International Meeting on Information Display (IMID), Daegu, Korea, 26 to 29 August 2013.
26. D. Yang, D. Ma, 1,1-Bis[(di-4-tolylamino)phenyl]cyclohexane for fast response organic photodetectors with high external efficiency and low leakage current. *J. Mater. Chem. C* **1**, 2054–2060 (2013).
27. A. N. Bashkatov, E. A. Genina, V. V. Tuchin, Optical properties of skin, subcutaneous, and muscle tissues: A review. *J. Innovative Opt. Health Sci.* **4**, 9–38 (2011).
28. A. N. Bashkatov, E. A. Genina, V. I. Kochubey, V. V. Tuchin, Optical properties of human skin, subcutaneous and mucous tissues in the wavelength range from 400 to 2000 nm. *J. Phys. D. Appl. Phys.* **38**, 2543 (2005).
29. M. J. C. van Gemert, S. L. Jaques, H. J. C. M. Sterenborg, W. M. Star, Skin optics. *IEEE Trans. Biomed. Eng.* **36**, 1146–1154 (1989).
30. R. R. Anderson, J. A. Parrish, Optical properties of human skin, in *The Science of Photomedicine*, J. D. Regan, J. A. Parrish, Eds. (Plenum Press, 1982), pp. 147–194.
31. H.-W. Lee, J.-W. Lee, W.-G. Jung, G.-K. Lee, The periodic moving average filter for removing motion artifacts from PPG signals. *Int. J. Ctrl. Autom. Syst.* **5**, 701–706 (2007).
32. M. Kaltenbrunner, T. Sekitani, J. Reeder, T. Yokota, K. Kuribara, T. Tokuhara, M. Drack, R. Schwödiauer, I. Graz, S. Bauer-Gogonea, S. Bauer, T. Someya, An ultra-lightweight design for imperceptible plastic electronics. *Nature* **499**, 458–463 (2013).
33. J. Kim, P. Gutruf, A. M. Chiarelli, S. Y. Heo, K. Cho, Z. Q. Xie, A. Banks, S. Han, K.-I. Jang, J. W. Lee, K.-T. Lee, X. Feng, Y. G. Huang, M. Fabiani, G. Gratton, U. Paik, J. A. Rogers, Miniaturized battery-free wireless systems for wearable pulse oximetry. *Adv. Funct. Mater.* **27**, 1604373 (2017).
34. S.-I. Park, Y. Xiong, R.-H. Kim, P. Elvikis, M. Meitl, D. -H. Kim, J. Wu, J. Yoon, C.-J. Yu, Z. Liu, Y. Huang, K.-c. Hwang, P. Ferreira, X. Li, K. Choquette, J. A. Rogers, Printed assemblies of inorganic light-emitting diodes for deformable and semitransparent displays. *Science* **325**, 977–981 (2009).
35. J. Yoon, A. J. Baca, S.-I. Park, P. Elvikis, J. B. Geddes III, L. Li, R. H. Kim, J. Xiao, S. Wang, T.-H. Kim, M. J. Motala, B. Y. Ahn, E. B. Duoss, J. A. Lewis, R. G. Nuzzo, P. M. Ferreira, Y. Huang, A. Rockett, J. A. Rogers, Ultrathin silicon solar microcells for semitransparent, mechanically flexible and microconcentrator module designs. *Nat. Mater.* **7**, 907–915 (2008).
36. J. Yoon, S. Jo, I. S. Chun, I. Jung, H.-S. Kim, M. Meitl, E. Menard, X. Li, J. J. Coleman, U. Paik, J. A. Rogers, GaAs photovoltaics and optoelectronics using releasable multilayer epitaxial assemblies. *Nature* **465**, 329–333 (2010).
37. R.-H. Kim, D.-H. Kim, J. Xiao, B. H. Kim, S.-I. Park, B. Panilaitis, R. Ghaffari, J. Yao, M. Li, Z. Liu, V. Malyarchuk, D. G. Kim, A.-P. Le, R. G. Nuzzo, D. L. Kaplan, F. G. Omenetto, Y. Huang, Z. Kang, J. A. Rogers, Waterproof AlInGaP optoelectronics on stretchable substrates with applications in biomedicine and robotics. *Nat. Mater.* **9**, 929–937 (2010).
38. V. V. Tuchin, *Tissue Optics: Light Scattering Methods and Instruments for Medical Diagnosis* (SPIE Press, 2007), vol. 13.
39. S. Mladenovski, K. Neyts, D. Pavicic, A. Werner, C. Rothe, Exceptionally efficient organic light emitting devices using high refractive index substrates. *Opt. Express* **17**, 7562–7570 (2009).


**Acknowledgments:** We are grateful to T. Kondo at LINTEC Co. Ltd. for supplying precoated gas barrier PET films. We also thank K. Song at Healthrian Co. Ltd. (Korea) and his research colleague for assistance in $SpO_2$ measurement. **Funding:** This research was supported in part by the Nano·Material Technology Development Program through the National Research Foundation of Korea (NRF) funded by the Ministry of Science, ICT and Future Planning (NRF-2016M3A7B4910631), and the Engineering Research Center of Excellence Program supported by the National Research Foundation (NRF), Korean Ministry of Science, ICT and Future Planning (MSIP) (NRF-2017R1A5A1014708). **Author contributions:** H.L. and S.Y. conceived the overall idea and designed the experiments. E.K. and H.L. performed the optical simulation. H.L. and J.L. fabricated the OLED devices, and H.L., H.K., and M.K. designed and fabricated the OPD devices. Y.L. and H.-J.Y. realized the integrated circuit for signal processing. H.L., E.K., and S.Y. wrote most of the manuscript. H.L. performed most of the characterization unless specified otherwise. All authors read and commented on the manuscript. **Competing interests:** S.Y. and H.L. are inventors on two Korean patent applications related to this work (no. 10-2018-0036210, filed on 29 March 2018, and no. 10-2018-0037002, filed on 30 March 2018). The other authors declare that they have no competing interests. **Data and materials availability:** All data needed to evaluate the conclusions in the paper are present in the paper and/or the Supplementary Materials. Additional data related to this paper may be requested from the authors.

Submitted 11 January 2018
Accepted 3 October 2018
Published 9 November 2018
10.1126/sciadv.aas9530

**Citation:** H. Lee, E. Kim, Y. Lee, H. Kim, J. Lee, M. Kim, H.-J. Yoo, S. Yoo, Toward all-day wearable health monitoring: An ultralow-power, reflective organic pulse oximetry sensing patch. *Sci. Adv.* **4**, eaas9530 (2018).